

Water Resources Research

RESEARCH ARTICLE

10.1029/2019WR025420

Key Points:

- Image processing of a microfluidic chip experiment provides insights on the pore-scale characteristics of biominerals in porous media
- The results of image analysis are significantly affected by the assumed particle shape, being cylindrical or semispherical
- Observed cumulative crystal volume, bulk precipitation rate, number of crystals, and crystal size distribution deviate from expected values

Correspondence to:

L. A. van Paassen,
leon.vanpaassen@asu.edu

Citation:

Kim, D. H., Mahabadi, N., Jang, J., & van Paassen, L. A. (2020). Assessing the kinetics and pore-scale characteristics of biological calcium carbonate precipitation in porous media using a microfluidic chip experiment. *Water Resources Research*, 56, e2019WR025420. <https://doi.org/10.1029/2019WR025420>

Received 23 APR 2019

Accepted 3 FEB 2020

Accepted article online 05 FEB 2020

Assessing the Kinetics and Pore-Scale Characteristics of Biological Calcium Carbonate Precipitation in Porous Media using a Microfluidic Chip Experiment

Daehyun H. Kim^{1,2} , Nariman Mahabadi^{1,3} , Jaewon Jang⁴ , and Leon A. van Paassen¹ 

¹School of Sustainable Engineering and the Built Environment, Arizona State University, Tempe, AZ, USA, ²Laboratory of Soil Mechanics, École Polytechnique Fédérale de Lausanne, Lausanne, Switzerland, ³Department of Civil Engineering, University of Akron, Akron, OH, USA, ⁴Department of Civil and Environmental Engineering, Hanyang University, Seoul, Korea

Abstract Biomineralization through microbially or enzymatically induced calcium carbonate precipitation (MICP/EICP) by urea hydrolysis has been widely investigated for various engineering applications. Empirical correlations relating the amount of mineral precipitation to engineering properties like strength, stiffness, or permeability show large variations, which can be partly attributed to the pore-scale characteristics of the precipitated minerals. This study aimed to gain insight into the precipitation kinetics and pore-scale characteristics of calcium carbonate minerals through time lapse imaging of a transparent microfluidic chip, which was flushed 10 times with a reactive solution to stimulate EICP. An image processing algorithm was developed to detect the individual precipitated minerals and separate them from the grains and trapped air. Statistical analysis was performed to quantify the number and size distribution of precipitated minerals during each treatment cycle and the cumulative volume, surface area, bulk precipitation rate, nucleation rate, and supersaturation were calculated and compared with a simple numerical model and more complex theory on precipitation kinetics. The analysis showed that results were significantly affected by the assumed particle shape. The supersaturation, which controls the crystal nucleation and growth rates, was shown to be a function of the hydrolysis rate, the kinetic order and growth rate constant, and available surface area for mineral growth. Possible explanations for observed discrepancies between observations and theory, including diffusion limitations, the presence of inhibiting compounds, local pore clogging or observation bias, and limitations of the methodology, are discussed.

1. Introduction

Biomineralization has potential for various engineering applications, for example, improving soil strength (Phillips et al., 2013; Van Paassen, 2009; Whiffin et al., 2007), reducing the hydraulic conductivity of soils (Nemati & Voordouw, 2003; Zhang et al., 2010), immobilizing groundwater contaminants (Ferris et al., 2004; Fujita et al., 2004), enhancing oil recovery (Cunningham et al., 2009), increasing storage security of CO₂ (Cunningham et al., 2011), and fugitive dust control (Hamdan & Kavazanjian, 2016). Biomineralization can be stimulated through microbially or enzymatically induced calcium carbonate precipitation (MICP or EICP) by stimulating urea hydrolysis in the presence of dissolved calcium ions. Urea hydrolysis is a slow irreversible reaction, which can be catalyzed by the enzyme urease. The urea is dissolved in water and hydrolyzes into ammonia and inorganic carbon. In aqueous solution, the ammonia is in equilibrium with ammonium, while the inorganic carbon can be present as carbon dioxide, bicarbonate, or carbonate depending on pH, or it can form complex ions in combination with calcium. At neutral pH, the dominant species are ammonium and bicarbonate and the overall reaction of urea hydrolysis is



The pH increases as hydroxide is generated to maintain the charge balance. An increase in pH causes bicarbonate to dissociate to carbonate and release a proton.



And in the presence of sufficient calcium ions, calcium carbonate will precipitate.



The acid released due to speciation and precipitation buffers the alkalinity production from the hydrolysis reaction, and consequently, the pH remains around neutral. As the precipitated biominerals fill the pore space, they will reduce porosity and permeability, and by forming cementing bonds between the grains in granular soils, they may increase strength and stiffness of the soil matrix.

The design of engineering applications of MICP or EICP processes relies on availability of predictive models. However, since modeling of EICP in natural soil systems involves multiphase reactive transport, nonlinear reaction kinetics and interactive coupled processes, this is a challenging task (Burbank et al., 2013; Hommel et al., 2016; Minto et al., 2019). Several numerical models have been developed, of which some have been validated using experimental studies. These studies have interpreted the process at different scales including pore scale (Kim et al., 2017; Mahabadi et al., 2017; Qin et al., 2016), column scale (Barkouki et al., 2011; Martinez et al., 2011), meter scale (Nassar et al., 2018), and large scale (van Wijngaarden et al., 2011, 2012, 2013). The geochemical processes for MICP can be modeled with different levels of complexity. Simplified models describe the process using a single chemical reaction equation, which combines equations (1), (2), and (3) (Cuthbert et al., 2013; Hommel et al., 2015, 2016). More advanced models include geochemical speciation reactions of the different solute species often by using specific geochemical speciation software packages such as PHREEQC (Charlton & Parkhurst, 2011; Parkhurst & Appelo, 2013), Orchestra (Salek et al., 2016; Ubbink, 2013), or TOUGHREACT (Barkouki et al., 2011). Some of these models included precipitation kinetics, describing the nucleation and growth rate of CaCO_3 minerals (e.g., Barkouki et al., 2011, Ebigbo et al., 2012, Qin et al., 2016). Van Paassen (2009) showed that biochemical conversion can be reasonably well predicted, using a simplified single reaction approach, in which the substrate concentrations, and kinetics of urea hydrolysis are used as input variables. However, more complex models are required to predict pH, supersaturation, and resulting characteristics of precipitated minerals. However, quantitative prediction to a level at which the pH, the supersaturation, and the number, size, and type of crystals are simulated accurately has not yet been possible. Such complex modeling would require to determine parameters, which describe the kinetics of urea hydrolysis, such as the maximum urease activity, substrate affinity, product inhibition, or enzymatic decay, and describe the kinetics of mineral nucleation and growth. Typically, these parameters are hard to be determined a priori, particularly in a complex poorly mixed environment such as porous media and they need to be fitted mathematically to experimental results.

Empirical relationships have been established, relating the amount of calcium carbonate to engineering properties, i.e. porosity, permeability, strength, or stiffness (Al Qabany et al., 2011; Burbank et al., 2013; Mortensen et al., 2011; Terzis & Laloui, 2018; Van Paassen, 2009; Whiffin et al., 2007; Zhao et al., 2014). However, these empirical correlations exhibit large variability (Terzis & Laloui, 2018; van Paassen et al., 2010; Yasuhara et al., 2012). The observed variability in the engineering properties of the treated soils depends on many factors. The characteristics of precipitated carbonate minerals, such as the amount, size, mineral type, shape, texture, location, and distribution, have been found to significantly affect the mechanical response (Almajed et al., 2019; DeJong et al., 2010). Many studies have used Scanning Electron Microscopy (SEM) images to analyze the characteristics of carbonate minerals formed through MICP or EICP (e.g., Al Qabany et al., 2011; Almajed et al., 2019; DeJong et al., 2010; Van Paassen, 2009). DeJong et al. (2010) analyzed SEM images of a thin cross section of MICP treated sands and suggested that the failure mechanism depended on the precipitation pattern. Van Paassen (2009) found that mineral type, size, and spatial distribution can vary depending on the precipitation conditions. Although high-resolution imaging tools, such as SEM, atomic force microscopy (AFM), or transmission electron microscopy (TEM), can provide valuable information about mineral type and structure, they are not capable of monitoring the MICP process during treatment and do not provide statistically quantifiable information about the spatial and property distribution of the precipitated minerals throughout a larger porous domain. Alternatively, microfluidic chips have been used to investigate precipitation kinetics and crystal characteristics of calcium carbonate in porous media (Dawe & Zhang, 1997; Wang et al., 2019; Yoon & McKenna, 2012; Zhang et al., 2010). Dawe and

Zhang (1997) developed a method in which they could observe crystal nucleation and growth inside a microfluidic chip under constant supersaturation conditions. They investigated the effects of the solution composition, temperature and the presence of a gas-liquid interface on the spontaneous nucleation and the calcite crystal growth rate. Zhang et al. (2010) used a microfluidic chip to study precipitation induced by transverse mixing of two separated solutions containing calcium and carbonate. The results were compared to numerical simulations by Yoon and McKenna (2012). Wang et al. (2019) used microfluidic chips to study the formation of calcite crystals by MICP. Using sequential microscopic images, with an image resolution of 0.65 $\mu\text{m}/\text{pixel}$, they were able to qualitatively describe the shape and size of the crystals, while varying the amount and composition of the injected solutions.

In this study, the growth and nucleation kinetics and resulting pore-scale characteristics of calcium carbonate minerals formed via EICP were explored by visual observation in a microfluidic chip. Experiments were performed at a larger scale than Wang et al. (2019), using an imaging system with a digital camera and microlens. An image processing algorithm was developed to analyze the experimental images and detect the growth of individual and agglomerated precipitated minerals with time for the entire microfluidic chip pore space. Statistical analysis was performed based on the processed images to assess the evolution of the number of precipitated minerals and their size distribution over time. Existing theory on crystal nucleation and growth and a simplified model describing the combined process of urea hydrolysis and calcium carbonate precipitation were used to interpret the results of the image analysis and provide insight on the kinetics of the precipitation process. The validity and limitations of using microfluidic chips for analysis of the precipitation kinetics are discussed.

2. Theoretical Background

2.1. Kinetics of Calcium Carbonate Precipitation

The amount, size, and mineralogy of calcium carbonate minerals depend on the kinetics of the precipitation process. The precipitation process can be divided in two separate mechanisms: crystal nucleation and crystal growth. Several models have been proposed to describe the rate of calcite crystal growth (e.g., Lasaga, 1981; Nancollas & Reddy, 1971; Noiriel et al., 2012; Söhnel & Garside, 1992). A general equation for the bulk precipitation rate, r_p , ($\text{kmol m}^{-3} \text{h}^{-1}$) is often described as

$$r_p = k_p(S-1)^n, \quad (4)$$

in which k_p is the bulk kinetic “constant” (in $\text{kmol m}^{-3} \text{h}^{-1}$), S is the supersaturation, and n is the kinetic order. The kinetic order depends on the growth mechanism. For example, first-order expressions ($n = 1$) have been suggested to describe the kinetics of calcite growth (Kazmierczak et al., 1982; Nancollas & Reddy, 1971), for example, when the crystallization process is limited by adsorption of lattice ions (Nielsen, 1984) or when the rate is controlled by diffusion (Pokrovsky et al., 2005). Second-order expressions ($n = 2$) are introduced to describe growth at screw dislocations by the spiral mechanism theoretically (Blum & Lasaga, 1987; Ganor & Lasaga, 1998) and have been measured experimentally (Reddy & Nancollas, 1973; House, 1981; Shiraki & Brantley, 1995). The second-order expression is suggested to describe the precipitation rate for supersaturated solutions, where S is close to 2 while the pH of solution is above 7 (Dawe & Zhang, 1997; Davies & Jones, 1955). Different orders of expressions have been reported (Söhnel & Mullin, 1982) but were not considered in this study. The supersaturation S is defined as

$$S = \sqrt{\frac{IAP}{K_{sp}}}, \quad (5)$$

where IAP is the ionic activity product of the dissolved precipitating ions (calcium and carbonate) and K_{sp} is the solubility product of the mineral phase. Calcium carbonate is a polymorph, which implies that the crystal lattice can have varying configurations. The most common and stable calcium carbonate minerals are calcite and aragonite. Aragonite may form when the growth of calcite is inhibited due to the presence of dissolved ions, such as magnesium and strontium (Hill et al., 1997; Morse, 1983; Perdikouri et al., 2013). Vaterite and amorphous calcium carbonate (ACC) are meta-stable calcium carbonate minerals, and calcium carbonate monohydrate and ikaite are calcium carbonate minerals that have water molecules incorporated

in their crystals lattice. The solubility product depends on the mineral type and varies with temperature (Gal et al., 1996; Plummer & Busenberg, 1982). For example, at 25 °C, K_{sp} is $10^{-8.48}$ for calcite, $10^{-8.34}$ for aragonite, $10^{-7.91}$ for vaterite, and $10^{-6.40}$ for ACC (Gal et al., 1996; Plummer & Busenberg, 1982; Sass et al., 1983). Due to their higher solubility product, the meta-stable precursor minerals typically can only occur under conditions of very high supersaturation and may dissolve and recrystallize into a more stable polymorph.

The bulk kinetic “constant,” k_p , is in fact not a constant but a function of the growth mechanism, mineral type, crystal surface area, and number of crystals:

$$k_p = \frac{k_g A_T}{V_m} = \frac{k_g A_c N}{V_m}, \quad (6)$$

in which k_g is the actual crystal growth rate constant in (m s^{-1}), A_T is the total crystal surface area (m^2), A_c is the average single crystal surface area (m^2), N is the number of crystals in (m^{-3}), and V_m is the molar volume of the crystallizing solid in ($\text{m}^3 \text{ kmol}^{-1}$), which is the ratio between molar mass (M_c) (in g mol^{-1}) and solid density (ρ_c) (in g m^{-3}). For calcite, $M_c = 100$ (kg kmol^{-1}), $\rho_c = 2,710$ (kg m^{-3}), and consequently $V_m = 0.0369$ ($\text{m}^3 \text{ kmol}^{-1}$) (Graf, 1961). The growth rate constant, k_g , in (m s^{-1}) depends on the mineral type, ionic strength of the solution, and temperature. At 25 °C, k_g is about $1 \cdot 10^{-11}$ (m s^{-1}) for calcite and $6 \cdot 10^{-10}$ (m s^{-1}) for vaterite (Kralj et al., 1997). No growth rate constants have been reported for ACC. Both A_c and N can vary in time during the biomineral formation process. The overall precipitation rate constant is proportional to the total surface area, A_T , of precipitated minerals over the solution volume (Appelo & Postma, 2004), in which A_T is the sum of surface areas of each individual crystal.

Nucleation, that is, the formation of new crystals, occurs when the solution becomes sufficiently supersaturated that clusters of dissolved molecules coagulate and get a critical size, which enables them to resist the tendency to redissolve, and allows them to start growing as a solid crystal. When nuclei appear in a pure liquid phase this is called homogeneous, spontaneous, or primary nucleation. Classical nucleation theory suggests that the rate of homogeneous nucleation for a spherical cluster of molecules is described using an Arrhenius equation, in which the activation energy, ΔG_{crit} , needs to be exceeded before nuclei can start to grow (Mullin, 2001):

$$J = \frac{dN}{dt} = A \exp \left[-\frac{G_{crit}}{kT} \right] = A \exp \left[-\frac{16\pi\gamma^3\nu^2}{kT^3(kT(\ln S))^2} \right], \quad (7)$$

where J is the nucleation rate (in $\text{m}^{-3} \text{ s}^{-1}$), A is the pre-exponential constant (in $\text{m}^{-3} \text{ s}^{-1}$), γ is the interfacial tension (in J m^{-2}), ν is the molecular volume of CaCO_3 ($6.13 \times 10^{-29} \text{ m}^3$), k is Boltzman constant ($1.3805 \times 10^{-23} \text{ J K}^{-1}$), and T is temperature (K). The pre-exponential component, A , represents the frequency of collisions between reactant molecules and can be estimated following Nielsen (1964) but is typically assumed to be constant. In this study, we used $A \approx 10^{35.5}$ ($\text{m}^{-3} \text{ s}^{-1}$), following Söhnel and Mullin (1982). Assuming constant temperature at 298 K, the nucleation rate can be calculated for different values of surface tension, which has been reported to range from 7 to 280 (mJ m^{-2}) (Söhnel & Mullin, 1982). In this study, we selected several values: $\gamma = 0.029 \text{ J m}^{-2}$ in the presence of polymeric substrate (Dalas et al., 1988) to $\gamma = 0.064$ or 0.098 J m^{-2} at which spontaneous nucleation occurs in a homogeneous solution in absence of nucleation sites (Lioliou et al., 2007; Söhnel & Mullin, 1982) or $\gamma = 0.120 \text{ J m}^{-2}$ in the presence of impurities which inhibit nucleation (Söhnel & Mullin, 1982). This equation indicates that theoretical nucleation rates may vary extremely, depending on the supersaturation and the presence of compounds, which either lower or increase the interfacial tension, and illustrates the difficulty to properly predict the rate of precipitation in case of spontaneous nucleation. On top of that, in the presence of seed crystals or other surfaces such as bacteria, enzymes, gas bubbles (Dawe & Zhang, 1997) or other minerals, which can act as a crystal nucleus, new crystals can appear through heterogeneous nucleation. In this case, the activation energy for nucleation reduces by the presence of seed crystals or other nucleation sites. Not all the minerals can act as a nucleus. For example, Lioliou et al. (2007) showed that quartz was hardly active as a nucleation site, while calcite obviously did. Consequently, in the presence of calcite seeds, heterogeneous nucleation can take place at lower supersaturation or nucleation can be skipped completely (Lioliou et al., 2007; Qin et al., 2016; Tai & Chen, 1995). The impact of bacterial cell surfaces as nucleation sites on the morphology, mineralogy, and size of CaCO_3 precipitation has been also

discussed (Mitchell & Ferris, 2006). Once crystals are present in the solution, their growth rate depends on the supersaturation and can be predicted using equations (4) and (6) above, where the crystal growth rate constant can vary depending on the type of calcium carbonate mineral phase.

2.2. Numerical Model Describing the Kinetics of EICP

Various numerical models have been developed to describe the kinetics of MICP or EICP, with increasing levels of complexity (Minto et al., 2019). The simplest models describe the hydrolysis and precipitation reaction as a single reaction, combining equations (1) to (3) (e.g., Cuthbert et al., 2013; van Wijngaarden et al., 2016; Hommel et al., 2015, 2016; Cunningham et al., 2019; Minto et al., 2019). Although these simplified models have been proven to predict the total amount of precipitated CaCO_3 reasonably correct, prediction of supersaturation and related crystal growth and nucleation kinetics requires to include solute speciation reactions and kinetic relationships to describe crustal nucleation and growth.

The hydrolysis rate is a function of several factors including the amount and source of urease enzyme, concentration of urea, calcium, pH, temperature, and other environmental conditions, such as the presence of inhibiting compounds and salinity (e.g., Fidaleo & Lavecchia, 2003; Hammes et al., 2003; Hammes & Verstraete, 2002; Lauchnor et al., 2015; Mortensen et al., 2011; Stocks-Fischer et al., 1999; Van Paassen, 2009; Whiffin, 2004). The observed urease activity in EICP or MICP experiments is often lower than expected. Flocculation or flush out of enzymes may reduce the available amount of enzymes in the porous medium, or the hydrolysis rate may decrease in time, as a result of decay or encapsulation of the bacteria or enzymes into a crystal lattice.

When combining hydrolysis of urea and precipitation of calcium carbonate, the rate of precipitation and the characteristics of resulting precipitated CaCO_3 minerals will depend on the hydrolysis rate, as the hydrolysis and precipitation reactions are coupled. Van Paassen (2009) demonstrated through batch experiments and numerical simulations that once nucleation has occurred and there is still sufficient calcium present in the solution, the hydrolysis rate and bulk precipitation rate are approximately equal during the major part of the reaction.

$$r_h \approx r_p \quad (8)$$

This suggests that the bulk precipitation rate can be predicted if the hydrolysis rate is known, and by combining and inverting equations (4) and (6), it can be deduced that the supersaturation is a function of the hydrolysis rate:

$$S = \sqrt[n]{\frac{r_p V_m}{k_g A_T} + 1} \quad (9)$$

This implies that at low hydrolysis rates, precipitation occurs at relatively low supersaturation, while at high hydrolysis rates, supersaturation is relatively high and may remain high for a prolonged period of time. Conditions of prolonged high supersaturation may extend growth of meta-stable CaCO_3 minerals, such as amorphous CaCO_3 or vaterite, which was demonstrated by Van Paassen (2009) and Al-Thawadi and Cord-Ruwisch (2012).

In this study, we used a simplified model to predict the cumulative volume of precipitated minerals, following, for example, Van Paassen (2009), Fidaleo and Lavecchia (2003), van Wijngaarden et al. (2011), Connolly et al. (2013), Lauchnor et al. (2015), and Minto et al. (2019). Using the applied amount of substrates and enzymes and the urease activity provided by the manufacturer as input parameters and assuming hydrolysis and precipitation rate are equal, the reaction rate is described using the equation:

$$r_h = r_p = v_{max} \frac{C_s}{K_m + C_s} \quad (10)$$

in which r_h is the hydrolysis rate, v_{max} is the maximum urease activity (in $\text{mol L}^{-1} \text{hr}^{-1}$) as provided by the manufacturer's specifications, C_s is the concentration of the substrate urea (in mol L^{-1}), and K_m is the half saturation coefficient (affinity constant) in (mol L^{-1}).

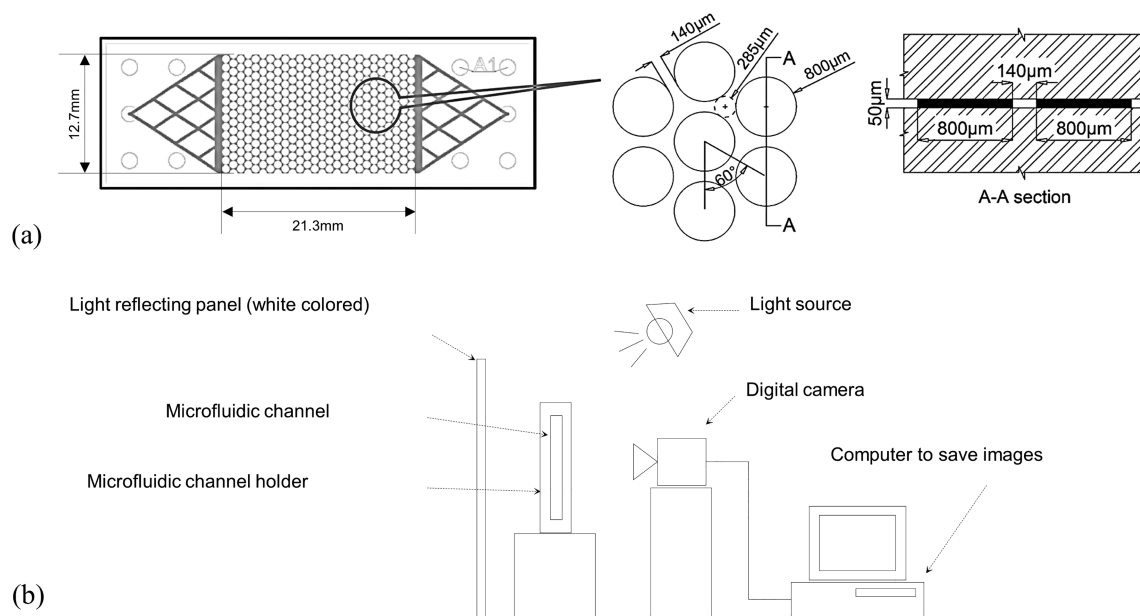


Figure 1. (a) Geometry of the patterned microfluidic chip (Mahabadi et al., 2016; Zheng et al., 2017). (b) Experimental configuration of the microfluidic chip test.

3. Experimental Study

3.1. Preparation of Reactive Solution

The reactive solution prepared in this study was based on Nemati and Voordouw's (2003) experimental work and contained 12 g (~ 200 mmol L^{-1}) urea ($CO(NH_2)_2$, U5378, Sigma-Aldrich), 30 g (~ 200 mmol L^{-1}) calcium chloride dihydrate ($CaCl_2 \cdot 2H_2O$, C3881, Sigma-Aldrich), and 0.1 g (~ 0.01 w%) urease powder (extracted from jack beans, Type III, 26100 [U g^{-1}], U1500, Sigma-Aldrich) per liter. DI water was used to prepare the solution. Consequently, the concentrations of both urea and calcium chloride were at a 1:1 molar ratio and the expected maximum urease activity, $v_{max} \approx 0.078$ (mol-urea $L^{-1} hr^{-1}$). Unlike Nemati and Voordouw's recipe, the solution did not include milk powder.

3.2. Microfluidic Chip Experiment

A two-dimensional transparent microfluidic chip (Micronit Microfluidics BV, The Netherlands) was used, which was designed and fabricated to resemble a homogenized circular particle packing (Mahabadi et al., 2016; Zheng et al., 2017). The dimension of the microfluidic chip is 21.3 mm \times 12.7 mm, and the internal thickness (pore depth) is 50 μm . The microfluidic chip includes 377 circular mono-sized grains with 800 μm of diameter, and the size of pore throat between two grains is 140 μm (Figure 1a). Figure 1b shows the configuration of the microfluidic chip experimental setup. The microfluidic chip with injection and extraction ports is fixed in a steel holder and placed vertically. Before the first flush, the microfluidic chip was air filled. The prepared solution was injected into from the bottom inlet. After the injection, both inlet and outlet ports were closed to prevent evaporation and fluid flow. The solution was left to react for 48 hr. The injection-reaction process was repeated 10 times. The volume of injected solution in each cycle was about 0.5 ml, which is significantly larger than the pore volume of the microfluidic chip to ensure the entire system volume would be replaced, including the volume of the tubing and inlet and outlet channels. After each flushing and reaction cycle, the microfluidic chip was flushed with about 0.5 ml of deionized water, to wash out the retained solution before injecting the next batch of EICP solution.

Time lapse digital photography was performed every 10 min for the entire reaction process (48 hr each cycle) to continuously monitor the evolution of carbonate mineral formation within the entire microfluidic chip. A digital camera (D5200, Nikon) equipped with a 60 mm microlens (AF-S Micro NIKKOR 60 mm f/2.8G ED, Nikon) was used to capture the growth of precipitated calcium carbonate minerals in high-resolution images.

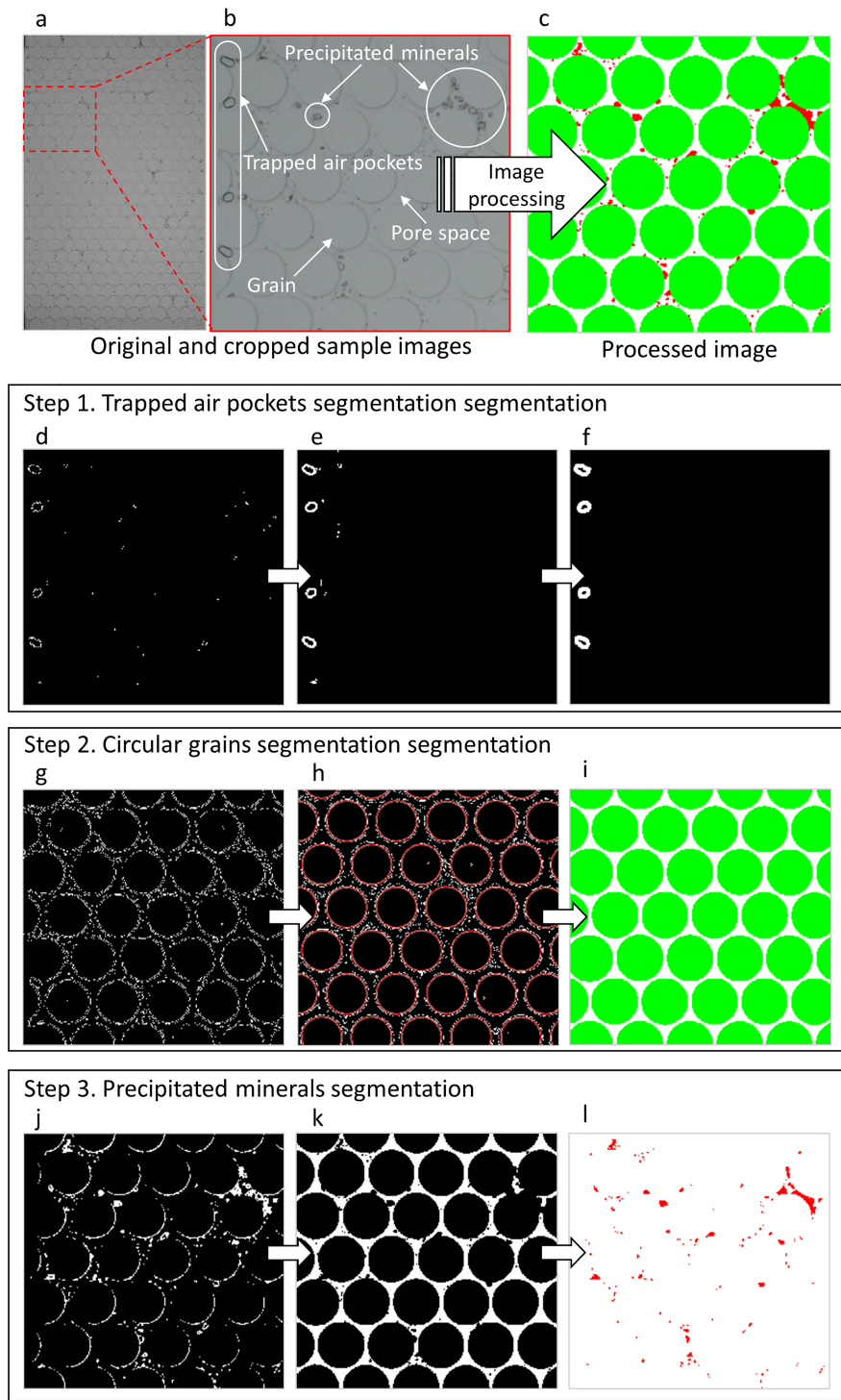


Figure 2. Phase segmentation performed by the automated image processing (top): (a) Original experimental sample image showing the entire domain of microfluidic chip; (b) cropped area from the sample image including different phases; and (c) processed image based on the image segmentation. Image processing algorithm (bottom): The algorithm mainly consists of three steps: (d–f) Detection of trapped air pockets; (g–i) detection of circular grains; and (j–l) detection of biominerals.

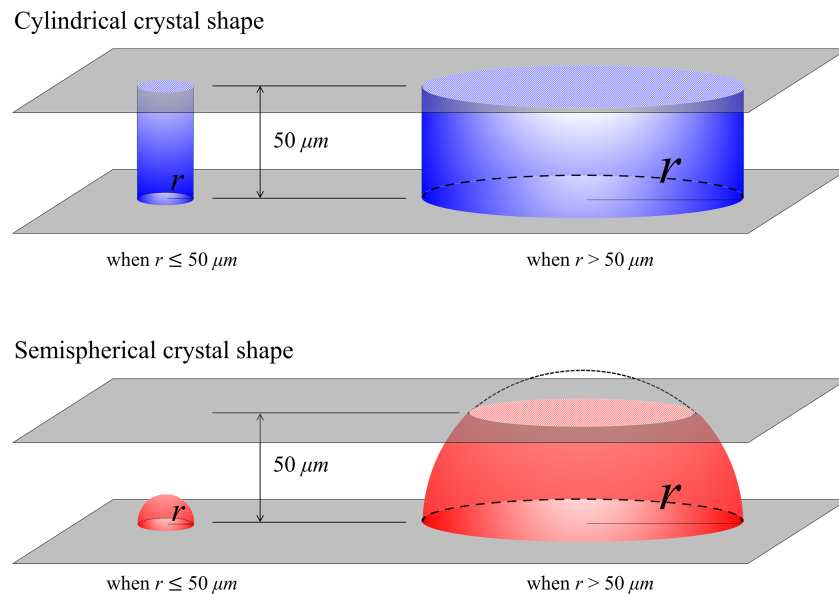


Figure 3. Two hypothetical shapes of calcium carbonate crystal formation in microfluidic chip.

3.3. Image Processing

A comprehensive image processing algorithm was developed using MATLAB (ver. R2017a) to automatically detect and extract the precipitated calcium carbonate crystals from the original images and monitor the precipitation process within the microfluidic chip over time. The proposed algorithm allows for a consistent detection of the boundaries of the different phases, minimizing human error associated with manual detection, thereby improving the reproducibility of the detection process, and significantly reduces the time for massive image data analysis. Figure 2a shows the raw image of the entire microfluidic chip at the end of fourth treatment cycle. Figure 2b highlights a cropped area of Figure 2a including the circular grains, precipitated minerals, and a few air bubbles which were trapped along the sides of the microfluidic chip. It should be noted that during the injection, some air bubbles were also flushed with the injected solution through the microfluidic chip. At the end of the injection, a few air bubbles were trapped in the low accessible pores along the left and right boundaries of the domain. Figure 2c shows the final processed image by an automated algorithm including the detected grains (presented in green color), precipitated minerals (presented in red color), and pore space (presented in white color). The detailed steps of the proposed image processing algorithm are explained as follows:

Image binarization: Image binarization is the first prerequisite for multiphase segmentation, which aims to detect the outlines of all different phases such as grains, minerals, and pores. Acquisition of desired information from a digital image requires the segmentation of objects in it. Every digital color image consists of three $n \times m$ Red, Green, and Blue (RGB) matrixes where n and m define the number of pixels in horizontal and vertical directions, and each pixel has a value ranging from 0 to 255. Converting the color image (RGB) to the gray-scale format (intensity image) allows to simply store all the information into a single matrix that facilitates post image segmentation processes. The digital RGB raw images of the microfluidic chip experiment were converted to gray-scale image and then turned into black and white (0 and 1) binary image by applying different intensity thresholds to classify different target objects (grains, minerals, and air pockets). The section below explains the image processing steps applied to detect the three different phases (air pockets, circular grains, and precipitated minerals):

Step 1. Detection of air pockets: In order to identify the location, size, and numbers of biominerals, unnecessary objects such as air bubbles and circular grains needed to be identified and removed from the images. Air bubbles were detected and stored in a separate binary image using the Roberts (1965) edge detection method (Figure 2d). However, in some cases the detected outlines of air bubbles include discontinuities. For this reason, we used another function *imdilate* in MATLAB that allows to reconstruct the continuous boundary

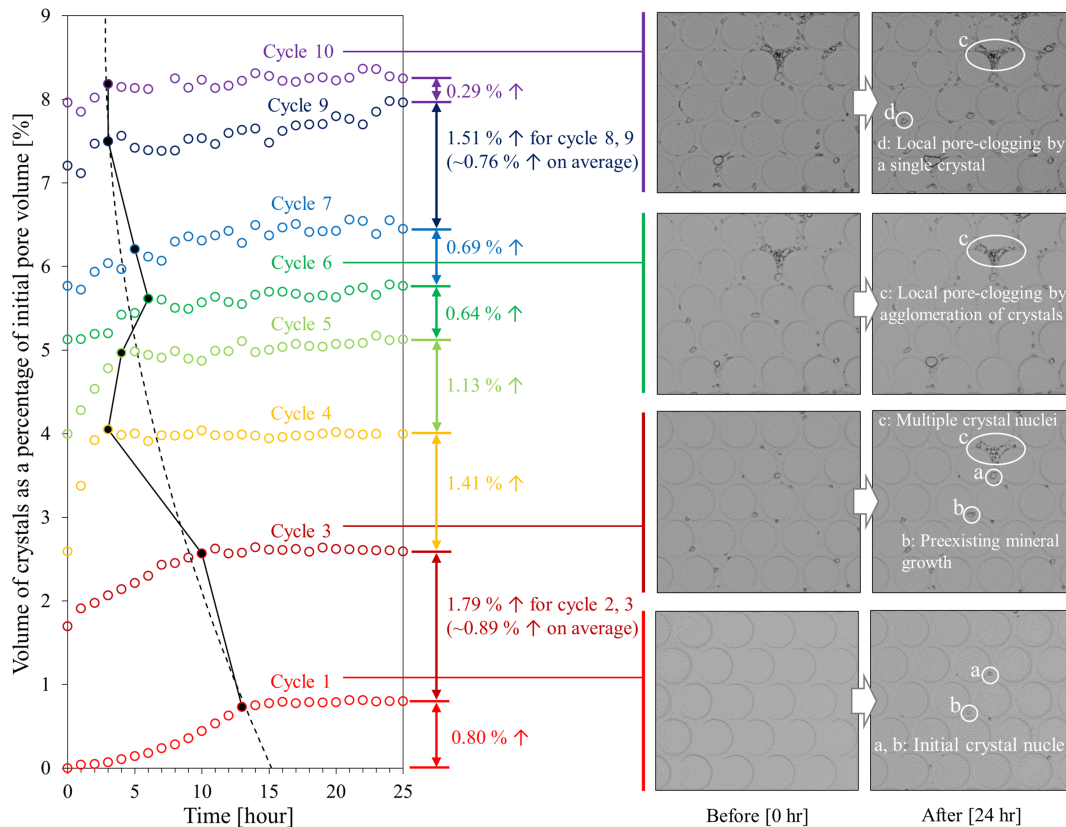


Figure 4. Volume of crystals as a percentage of initial pore volume with time for each cycle of treatment assuming cylindrical crystal shape (left). Highlighted area of the experimental images before and after EICP treatment for Cycles 1 (red), 3 (brown), 6 (green), and 10 (purple) (right).

around the disconnected air bubbles by dilating the boundary pixels (Figure 2f). The dilated reconstructed boundaries of bubbles were filled and then contracted to compose bubbles and return their expanded size to the original size. The detected bubbles were later removed from the binary image constructed in step 3 for mineral detection (Figure 2j).

Step 2. Detection of circular grains: The Canny (1986) edge detection method was applied to obtain the perimeter boundaries of circular grains (Figure 2g). This method uses a block to find edges by searching for local maxima of the gradient within the Gaussian filtered image. The Canny method finds two threshold values, a higher and lower threshold, to detect strong and weak edges, and includes the weak edges in the output only when they are connected to strong edges. By applying the Gaussian filter and judging connectivity between weak and strong edges, the Canny method is more likely to remove the noise and detect a wide range of edges with high sensitivity. Thereafter, the *imfindcircle* function in MATLAB was employed to find and record the center's coordination and diameter of circular grains (detected grains presented by red circles in Figure 2h). However, due to variations of brightness over the grains, the size of detected circles varied. Considering the fact that all the grains have a fixed size (800 μm), the size of the detected circular grains was adjusted to satisfy this constraint. Using the detected center and radius, the circular grains were mapped out and converted to a separate binary image (Figure 2i).

Step 3. Detection of precipitated minerals: The precipitated minerals have relatively smaller size than the circular grains and air bubbles, so edge detection methods are not proper to find the minerals. In order to detect the precipitated minerals, the gray-scale image was turned into a binary image by using Otsu's method, which automatically selects threshold and replaces all the values above a specified threshold with 1 (white) and all other values with 0 (black) (Otsu, 1979). Otsu's method can be readily carried out by using "imbinarize" function in MATLAB. However, since the gray-scale image contains an illumination gradient, the default Otsu's method produces a very poor result. Moreover, the intensities of some parts of the circular

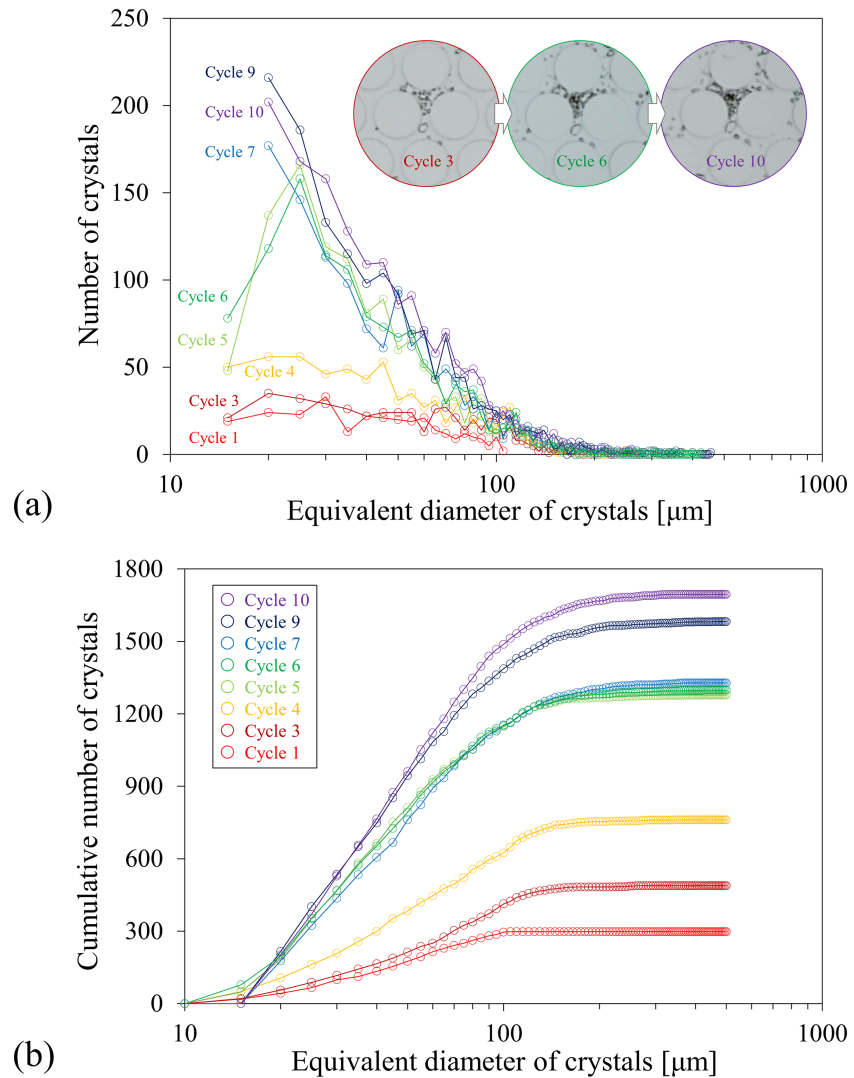


Figure 5. (a) Crystal size distribution at different flushing cycles and crystal formation-growth observation within the highlighted area of microfluidic chip (right upper). (b) Cumulative number of crystals for different cycles of treatment.

grain boundaries have similar values to those of the mineral boundaries. Therefore, Otsu's binarization method required some modification for precise detection of mineral boundaries. In order to minimize the illumination artifacts, localized thresholding was applied using the “adaptive” option within the “imbinarize” function. The “adaptive” method computes thresholds for each pixel using the local mean intensity of the neighborhood of the pixel. The “ForegroundPolarity,” “dark” option was used to detect the pixels occupied by mineral boundaries, considering the mineral boundaries have darker intensities than the background values. The threshold in this option can be specified by the ‘sensitivity’ parameter, which ranges between 0 and 1. A higher sensitivity identifies more pixels as mineral boundaries. Due to illumination changes during the different cycles, the threshold values may vary slightly and needed to be manually selected using a trial and error approach. For the image in Figure 2, the “sensitivity” was determined at 0.54 after trial and error. The resulting image (Figure 2j) still contained boundaries of circular grains. The detected circular grains in the previous step were redrawn, filled (Figure 2i) and overlapped onto Figure 2j, then the result was reversed. The reversed image included the circular grains and mineral outlines in black and pores in white but left the inside of some relatively big minerals white. These larger minerals, which were defined by their pixel size (<100), were filled black using the

“bwareaopen” function to obtain Figure 2k. By subtracting redrawn and filled grains (Figure 2i) from Figure 2k, the mineral phase could be generated as a separate phase (Figure 2l).

3.4. Statistical Analysis of the Mineral Phase

Quantitative information of the precipitated biominerals, that is, the size, number, and volume of crystals, were derived from the processed images (Figure 2l). In order to determine the individual crystal size, the number of pixels in each crystal were counted to determine the crystal area. Based on the size and resolution of the images, each pixel has the approximate dimensions of $6.5 \mu\text{m} \times 6.5 \mu\text{m}$. The equivalent diameter, d_{eq} , of the individual crystals was derived from the total area of pixels (A_p) using

$$d_{eq} = \sqrt{\frac{4A_p}{\pi}} \quad (10)$$

In order to exclude undesirable noises from the results, it was decided to exclude the detected crystals which were 3 pixels or less in size. This noise filtering may cause underestimating the volume of crystals.

The volume and crystal surface area of the individual crystals were calculated in different ways, depending on the assumption of the crystal shape. Assuming crystals had a cylindrical shape and filled up the entire internal thickness of the microfluidic chip, $h = 50 (\mu\text{m})$, crystals can only grow radially and the crystal surface area, A_c (in μm^2), and crystal volume, V_c (in μm^3), are calculated using

$$A_c = \pi h d_{eq} = 100\pi r_{eq} \text{ and } V_c = 50\pi r_{eq}^2 \quad (11)$$

Alternatively, assuming that crystals have a semispherical shape and are attached either to the front or the back of the microfluidic chip, the crystal height varies depending on the equivalent crystal radius. When the radius of a semispherical crystal is smaller than the internal thickness of the microfluidic chip, surface area and volume are calculated using

$$A_c = 2\pi r_{eq}^2 \text{ and } V_c = \frac{2}{3}\pi r_{eq}^3 \quad (12)$$

Once the radius of semispherical crystal is bigger than the internal thickness of the microfluidic chip, surface area and volume are calculated using

$$A_c = 100\pi r_{eq} \text{ and } V_c = \pi \left(50r_{eq}^2 - \frac{50^3}{3} \right) \quad (13)$$

The two hypothetical shapes are shown in Figure 3. The total volume of crystals and total surface area, A_t , are obtained by adding up the values for all individual crystals.

4. Results and Discussion

Figure 4 shows the results of image analysis. On the left side the volume of crystals is plotted as a percentage of the initial pore volume of the untreated microfluidic chip as a function of time assuming cylindrical crystal shapes. As results of 10 cycles of EICP treatment, the total volume of crystals filled up about 8.25% of the pore space. The change in crystal volume per cycle varied. From 0.80% in the first treatment cycle, it reached a maximum of 1.41% in the fourth cycle and then declined to 0.29% in the 10th cycle. The results of second and eight treatment cycles are not included as the images of these cycles were not sharp and could not be processed properly. The repetitive shutter operations of the digital camera during these cycles caused a slight movement of the test setup and a loss of focus of camera, which demonstrates that even a small disturbance during the image capturing process may critically affect the quality of the output images. In order to prevent this experimental issue, all imaging equipment including the camera, microfluidic chip, and light source are required to be completely fixed with a rigid frame during the experiment.

During each treatment cycle, the volume of crystals increased until a threshold was reached, after which no more crystal volume change was recorded. During the first cycle, a lag phase occurred, which lasted for ~5 hr

Table 1

The Bulk Precipitation Rate (r_p), Cumulative Crystal Surface Area (A_T), Number of New Crystals (N), and Nucleation Rate (dN/dt) for Each Treatment Cycle and Calculated Supersaturation (S) for Different Growth Constant (c : Calcite; v : Vaterite) and Kinetic Order (1: First Order; 2: Second Order)

Cycle	Cylindrical crystal shape						Semispherical crystal shape						Observation	
	r_p (kmolm ⁻³ h ⁻¹)	A_T (mm ²)	S_{c2} (-)	S_{v2} (-)	S_{c1} (-)	S_{v1} (-)	r_p (kmolm ⁻³ h ⁻¹)	A_T (mm ²)	S_{c2} (-)	S_{v2} (-)	S_{c1} (-)	S_{v1} (-)	N (-)	dN/dt (m ⁻³ s ⁻¹)
1	0.015	2.20	77.8	35.3	5,899	1,181	0.008	1.3	71.3	32.5	4,945	990	298	0.0064
3	0.024	4.83	65.7	29.9	4,182	837	0.015	3.6	59.4	27.1	3,414	683	95	0.0026
4	0.132	7.24	125.6	56.7	15,528	3,106	0.073	5.4	108.4	49.0	11,540	2,309	273	0.0253
5	0.066	10.1	75.7	34.4	5,579	1,117	0.029	6.6	62.4	28.5	3,768	754	517	0.0359
6	0.022	10.7	42.8	19.7	1,747	350	0.034	7.2	64.3	29.3	4,007	802	20	0.0009
7	0.024	11.5	43.1	19.8	1,776	356	0.027	7.9	55.1	25.2	2,928	586	30	0.0017
9	0.026	13.8	41.4	19.1	1,633	327	0.047	9.6	65.5	29.9	4,166	834	127	0.0118
10	0.020	15.0	34.6	16.0	1,127	226	-0.001	10.4	<1	<1	<1	<1	113	0.0105

(red hollow circles in Figure 4), after which the first crystals were detected. The volume of crystals gradually increased until about 14 hr, after which no further significant change in crystal volume was observed. The lag phase in the first cycle could be interpreted as an induction time in which the supersaturation first needs to increase sufficiently in order to trigger crystal nucleation. Another reason for the observed lag phase could be that the initial crystals were too small to be detected at the given image resolution. In subsequent cycles, the time to reach the end of reaction, which is indicated by the black-dashed line shown in Figure 4, decreased, which indicates that the bulk precipitation rate gradually increased with increasing number of cycles. Most significant change in bulk precipitation rate was observed within the first four cycles of treatment. After the fourth cycle, the precipitation rate remained approximately constant. The increase in bulk precipitation rate may be due to the presence of already existing crystals, which grow or stimulate heterogeneous nucleation and facilitate immediate precipitation, skipping the induction and nucleation phase. The precipitation rate can also be affected by differences in urease activity, substrate distribution, or amount of remaining substrates or enzymes from the previous cycles of treatment.

A detail of the original experimental images for the first, third, sixth, and 10th cycle is shown on the right side of Figure 4. These images illustrate the formation process of biominerals within subsequent treatment cycles. During the initial cycles of treatment, nucleation of new crystals is expected to occur. Small nuclei may have settled in the liquid but were too small to be detected. As soon as the crystals reached an observable size, no movement of crystals was observed. Examples of new crystal occurrences are highlighted with labelled white circles (labels *a* and *b*) for the first cycle of treatment. By tracking crystals, *a* and *b*, it is clear that individual crystals gradually grow as the treatment cycles increase (labels *a* and *b* from Cycles 1 to 3). In some cases, the growth of crystals leads to pore clogging. Pore clogging either could be the result of an agglomeration of multiple crystals (label *c*), not only due to a single large crystal (label *d*) but also due to a trapped gas bubble, or could reduce pore connectivity and affect the transport and distribution of substrates and resulting precipitates in subsequent flushes. Local pore clogging may potentially explain observed variations in engineering properties of treated soils reported in the literature (e.g., van Wijngaarden et al., 2016; Whiffin et al., 2007).

The size distribution of crystals after each cycle of treatment is presented in Figure 5a. In order to construct these curves, crystals were categorized into bins according to their equivalent diameter, with each bin representing a 5 μm range. As the objects with a size with 3 pixels or less were filtered out by the image processing, the counting started at 15 μm, which represents the bin between 15–20 μm. The crystal size distribution typically revealed a (truncated) exponential distribution, which gradually changed with multiple cycles of treatment. At the first cycle of treatment, the range of crystal sizes covered a relatively narrow range of equivalent diameters (15–105 μm). Upon subsequent flushes, the variation in crystal size became wider reaching 20–455 μm at the ninth cycle of treatment. Besides an increase in size, the number of crystals also increased with multiple cycles of treatment, which implies that nucleation of new crystals and growth of existing minerals took place simultaneously throughout each cycle. The number of crystals within the range of 20–60 μm

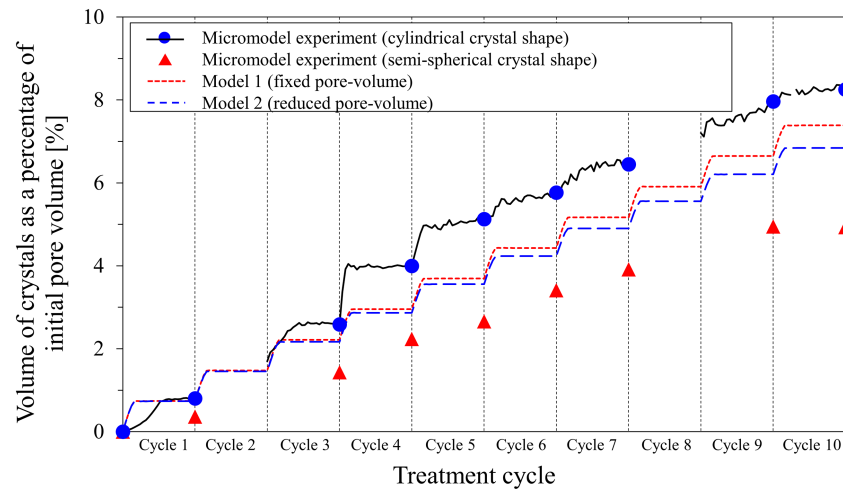


Figure 6. The estimated cumulative volume of crystals with increasing number of cycles based on the micromodel experiment using either cylindrical or semispherical crystal shape and the simulated cumulative volume of crystals based on the injected volume and concentrations of substrates and enzymes in the reactive solution assuming either a fixed pore volume (model 1) or pore volume reduction as a result of precipitation (model 2).

increased most significantly from the first cycle to fifth cycle, which confirms that nucleation of new crystals is most dominant within the first five cycles of treatment. After the fifth cycle, the predominant biomineralization mechanism is the growth of preexisting crystals.

The total number of crystals as shown in Figure 5b and Table 1 increased mostly within the first five cycles, particularly in the first, fourth, and fifth cycle. In the sixth and seventh cycles, the number of crystals did not significantly change, whereas in the ninth and tenth cycles, the total number of crystals increased again, but the increase in the number of crystals was smaller than in earlier cycles. This noticeable change in the cumulative number of crystals affirms that for all cycles of treatment, the precipitation mechanism involves both nucleation and growth. The results of statistical analysis were confirmed by the checking the original experimental images (right upper corner images in Figure 4a). The image representing Cycle 6 (green circle), clearly shows a number of new crystals are formed compared to the image of Cycle 3 (red circle), whereas the image of Cycle 10 (purple circle) shows that most of crystals have grown compared to Cycle 6, but the number of newly formed crystals is less. A reduction of the increase in number of crystals per cycle would be expected considering that preexisting crystals formed in previous cycles would stimulate heterogeneous nucleation or allow for crystal growth. Second, just like the total volume of crystals, the increase in number and size of crystals in each cycle would be affected by the accessibility of pore space when flushing substrate solution. After 5 cycles of treatment, some areas in the microfluidic chip become completely filled by precipitated biominerals, locally clogging the pores and creating inaccessible zones to the substrate solution, which would limit the growth or formation of new crystals in zones affected by those clogged regions.

Comparing the results with the numerical simulations showed several discrepancies. First, the increase in crystal volume for some of the cycles was significantly higher than theoretically possible when assuming cylindrical crystal shapes, particularly for Cycles 4 (1.41%) and 5 (1.13%). Also, the total volume of crystals after 10 treatment cycles (8.25%) was higher than expected. Simple mass and balance calculations indicate that for initial urea and calcium concentrations of $0.2 \text{ (mol L}^{-1}\text{)}$ and assuming complete conversion the maximum crystal volume increase is 0.74% of the initial pore volume. Considering that in each treatment cycle the pore volume is reduced by the volume of crystals, the theoretical increase in crystal volume reduces slightly each cycle reaching 0.69% in the 10th cycle. As a result of pore volume reduction, the total cumulative crystal volume after 10 cycles is expected to reach 7.15% instead of 7.4% when assuming a fixed pore volume, which was confirmed by the results of the simplified model simulations shown in Figure 6.

The crystal volume appeared to be significantly affected by the assumption that the precipitated minerals have a cylindrical shape and completely fill up the internal depth of the microfluidic chip. Considering

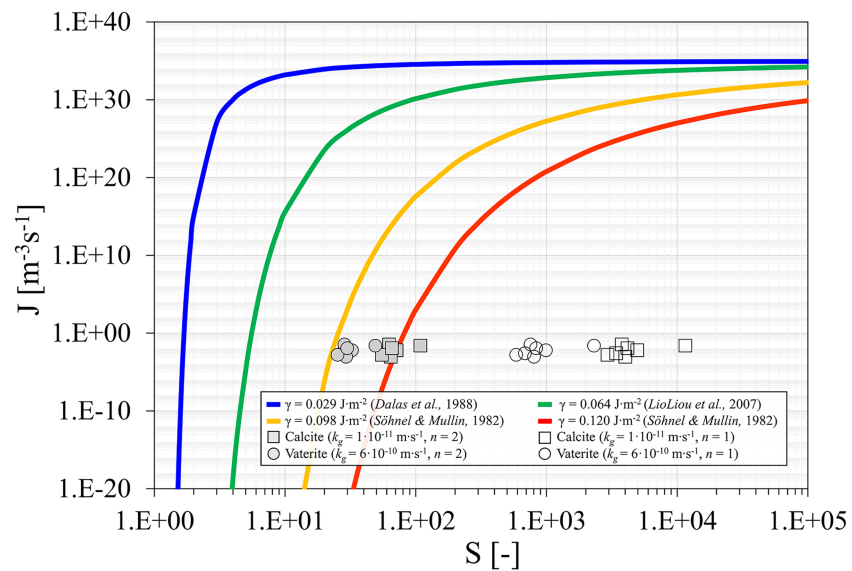


Figure 7. The theoretical and experimental nucleation rate for homogeneous nucleation of calcite crystals in S-J plot for various temperature and surface tension.

that smaller crystals may not fill up the entire depth of the microfluidic chip, the assumption of cylindrical crystal shape may overestimate the crystal volume. Calculating crystal volume assuming a semispherical crystal shape using equations ((12)) and ((13)) resulted in cumulative crystal volume that was on average 30% smaller compared to the values for cylindrical crystals. This difference may explain why the calculated volume increase during Cycles 4 and 5 in Figure 4 was larger than theoretically possible, particularly, because during these cycles, a large increase in the amount of new crystals was observed with relatively small sizes. The calculated cumulative crystal volume for semispherical crystal shapes was even lower than the results from the numerical model simulations. The difference between the model predictions and experimental observations assuming semispherical crystal shapes could be due to the local pore clogging, which creates zones within the pore volume, inaccessible for the convective supply of substrates and reduces the mobile pore volume, which causes a decrease of the amount precipitation. Further analysis on the effect of local pore clogging on substrate product distribution and porosity and permeability relationships in relation to EICP is required and currently being investigated. Other explanations for the differences between observed and predicted volumes may be the formation of alternative types and shapes of crystals or observation bias related to the limitations of the setup and image processing and analysis procedure, which is discussed later.

Table 1 provides a summary of the quantitative analysis of the statistical results, assuming either cylindrical or semispherical crystal shapes. The average bulk precipitation rate was calculated by dividing the amount of moles of CaCO_3 by the total time to reach full conversion (indicated by the black dots in Figure 5). The average bulk precipitation rate was in most cases lower than predicted, except for Cycle 4 assuming cylindrical crystal shape. Based on the amount of enzymes added and the specifications of the manufacturer, a maximum urease activity of $0.078 \text{ (mol m}^{-3} \text{ hr}^{-1})$ was expected. Similarly, Nemati and Voordouw (2003) or Whiffin et al. (2007) found that precipitation rates can be significantly lower than expected. The difference between the measured and expected precipitation rates could be due to various inhibition factors, as discussed in the theoretical background, but in this study, inaccuracies in the calculation of cumulative crystal volume and observation bias could contribute to this error. For example, part of the lag phase in the first cycle could be due to the fact that the initial crystals were still too small to be detected at the given image resolution. During the later flushes, the average precipitation rate may decrease as a result of local clogging, which reduces the available pore volume for convective supply of new substrates and consequently results in a lower increase in crystal volume.

The nucleation rate, dN/dt , was determined by dividing the increase in the number of observable crystals in each cycle, N , by the total reaction time. The reaction time in which crystal nuclei appear may range from

several seconds up to the total reaction time. It must be emphasized that the image resolution does not allow to observe the actual crystal nuclei as these would be far too small to be detected. Hence, the calculated dN/dt does not represent the actual nucleation rate but just the increase in the number of individual crystals in each cycle. Considering that each new crystal must have nucleated, the number of crystals may still be indicative of the amount of nuclei formed in each treatment cycle. Supersaturation was calculated following equation (9) using either a second- ($S2$ with $n = 2$) or first-order kinetic model ($S1$ with $n = 1$) and using the average bulk precipitation rate and total crystal surface area as an input. The growth rate constant, k_g , which depends on mineral type, was also varied from $1 \cdot 10^{-11}$ (m s^{-1}) for calcite to $6 \cdot 10^{-10}$ (m s^{-1}) for vaterite (Kralj et al., 1997). The total crystal surface area was calculated using either equation (11) for cylindrical crystal shape or equations (12) and (13) for semispherical crystal shape.

Figure 7 presents the calculated “nucleation rate” as a function of the calculated supersaturation for different model scenarios compares them with the theoretically expected nucleation rates based on classical nucleation theory according to equation (7) for different values of interfacial tension based on the values provided by Dalas et al. (1988), Lioliou et al. (2007), and Söhnel and Mullin (1982). The results of this comparison illustrate the sensitivity of the different parameters affecting the precipitation kinetics. Following equations (8) and (9), an increase in hydrolysis rate or decrease in crystal surface area increases supersaturation. Assuming first-order kinetics for the growth of calcite results in relatively high supersaturation, whereas second-order growth kinetics or growth of vaterite crystals reduces the supersaturation. Growth of ACC would result in even lower supersaturation, considering that the growth rate constant for ACC must be higher than for vaterite. Since the type of mineral cannot be easily distinguished at the given resolution, it is unclear, which mineral phase is predominant. However, the fact that, in each cycle, new crystals were observed indicates that local supersaturation must have been sufficiently high to allow for spontaneous nucleation.

Besides observation bias which is discussed later the low “nucleation rates” (or high supersaturations) may be due to inhibition of crystal nucleation. A minuscule amount of additives can significantly inhibit both of the nucleation and growth of calcium carbonate crystals (Bernard et al., 1992; Lin et al., 2005; Matty & Tomson, 1988; Söhnel & Mullin, 1982). The presence of dissolved organic matter may inhibit growth but favor nucleation (Lebron & Suarez, 1996). Proteins may also act as chelating compounds, lowering the concentration of free calcium ions, available for precipitation (Almajed et al., 2019). Second, the substrate solutions used in EICP experiments contain enzymes (i.e. organic polymers) of which the interaction with ions is not fully understood. And finally, precipitation in porous media takes place in a confined space, with limited convective mixing conditions and in the presence of heterogeneous surfaces. Hence, ion concentrations vary in space and time; the supersaturation can be affected by diffusion limitations or surface interaction and can often not be measured at pore scale. Therefore, both measurements and direct predictions of the supersaturation and the resulting precipitation kinetics and crystal characteristics formed by EICP should be interpreted with caution.

Quantitative interpretation of the results in this study is affected by significant observation bias and limitations in the setup or image analysis. First, the resolution of the images and the accuracy of the image analysis algorithm are limited. The resolution of the imaging setup used in this study does not allow to identify the small crystals or crystal nuclei. Hence, fluctuations in the volume, size, and number of crystals and derived parameters may be due to the inaccuracy of the processed images. Second, during the course of the experiment, more air bubbles got trapped during the injection of substrates, partly attributed to local clogging by the increased number and amount of biominerals. As a result, it became difficult to separate air bubbles from minerals, as the bubble-liquid meniscus were overlapping with crystal boundaries.

Another type of observation bias relates to the definition of nucleation versus growth. Crystal growth may occur as individual calcium and carbonate molecules are incorporated in the crystal lattice and by heterogeneous nucleation in which new individual crystals start growing on existing crystal surfaces. Once multiple crystals agglomerate, they cannot be distinguished as individual crystals as the image processing and quantitative analysis treats the agglomerated crystals as a single particle. As a result, the analysis may underestimate the number of individual crystals and the cumulative surface area. The resulting supersaturation and nucleation rate may also be underestimated.

Finally, the actual crystal shape may differ from the assumed cylindrical or semispherical crystal shapes. The actual crystal shape depends on the type of mineral, calcite, vaterite, or aragonite and the precipitation conditions. Vaterite typically shows spherical or “cauliflower” crystal shapes, while calcite typically forms single or clusters of rhombohedral crystals (e.g. Al-thawadi & Cord-Ruwisch, 2012; Van Paassen, 2009), but also dendritic calcite or aragonite crystal shapes have been observed (e.g. Pham et al., 2016). These different crystal shapes typically increase the surface area, which lowers the calculated supersaturation.

5. Conclusions

EICP by urea hydrolysis has been studied using a microfluidic chip experiment to gain insight in the growth and nucleation kinetics and pore-scale characteristics of CaCO_3 minerals. A reactive solution was flushed 10 times through a microfluidic chip and was allowed to react for 48 hr. The precipitation of CaCO_3 minerals was monitored by time sequential images. An image processing algorithm was developed to analyze the experimental images, assess the characteristics of the biominerals, and gain insight in the precipitation mechanisms and the kinetics of crystal nucleation and growth.

Despite a limited resolution, the cumulative crystal volume and bulk precipitation rate could be determined and corresponded reasonably well with values predicted with a simplified numerical model. The assumed crystal shape in the image analysis procedure significantly affected the calculated volume of crystals. Assuming a cylindrical crystal shape results in an overestimation of the crystal volume, particularly when the crystals are smaller than the internal thickness of the microfluidic chip. Assuming a semispherical crystal shape, the cumulative crystal volume and bulk precipitation rate were lower than expected and gradually decreased with an increasing number of cycles. This decrease can partly be attributed to local pore clogging, which reduces the mobile allowing a lower amount of substrate solution to be retained in the pore volume.

Also, the amount and size distribution of crystals could be determined. The fact that new crystals were observed in each treatment cycle indicated that in each cycle, supersaturation was high enough to allow for spontaneous nucleation of new crystals. The average supersaturation is estimated from the interpreted bulk precipitation rate and cumulative crystal surface area, for various scenarios in which growth rate constant and growth kinetic order are varied. Comparing the results with classical nucleation theory, it was found that for the calculated supersaturation, the observed “nucleation rates” were lower than expected. The variety between theoretical predictions and differences with experimental data emphasizes the difficulty to accurately predict the pore-scale characteristics of biominerals directly. Still, this study has shown that despite its limitations, the microfluidic chip can be used to estimate the bulk precipitation rate, cumulative crystal volume and surface area, and the size and spatial distribution for various process conditions. The microfluidic chip can therefore be a useful tool to assess the pore-scale characteristics of precipitated minerals in porous media. The proposed procedure can be used to optimize MICP or EICP treatment strategies or validate numerical models, by analyzing the effect of different substrate and enzyme concentrations and quantify relationships between pore-scale crystal characteristics and continuum scale “engineering” parameters of porous media, such as porosity and permeability.

Acknowledgments

Work described herein was supported in part by the National Science Foundation (NSF) Engineering Research Center program under Grant ERC-1449501. Any opinions, findings, and conclusions or recommendations expressed in this material are those of the authors and do not necessarily reflect those of the NSF. Authors would like to thank Prof. Tim Ginn and two anonymous reviewers for their critical feedback, which enabled to improve the manuscript. The datasets generated and analyzed during the current study, including the MATLAB scripts will be available in the Open Science Framework (OSF), at <https://osf.io/kprqd/>.

References

- Al Qabany, A., Soga, K., & Santamarina, C. (2011). Factors affecting efficiency of microbially induced calcite precipitation. *Journal of Geotechnical and Geoenvironmental Engineering*, 138(8), 992–1001.
- Almajed, A., Tirkolaei, H. K., Kavazanjian, E., & Hamdan, N. (2019). Enzyme induced biocemented sand with high strength at low carbonate content. *Scientific Reports*, 9(1), 1135. <https://doi.org/10.1038/s41598-018-38361-1>
- Al-Thawadi, S., & Cord-Ruwisch, R. (2012). Calcium carbonate crystals formation by ureolytic bacteria isolated from Australian soil and sludge. *Journal of Advanced Science and Engineering Research*, 2(1), 12–26.
- Appelo, C. A. J., & Postma, D. 2004. *Geochemistry, groundwater and pollution*. London, UK: CRC Press.
- Barkouki, T. H., Martinez, B. C., Mortensen, B. M., Weathers, T. S., de Jong, J. D., Ginn, T. R., et al. (2011). Forward and inverse biogeochemical modeling of microbially induced calcite precipitation in half-meter column experiments. *Transport in Porous Media*, 90(1), 23–39. <https://doi.org/10.1007/s11242-011-9804-z>
- Bernard, J. P., Adrich, Z., Montalto, G., De Caro, A., De Reggi, M., Sarles, H., & Dagorn, J. C. (1992). Inhibition of nucleation and crystal growth of calcium carbonate by human lithostathine. *Gastroenterology*, 103(4), 1277–1284.
- Blum, A. E., & Lasaga, A. C. (1987). Monte Carlo simulations of surface reaction rate laws. IN: *Aquatic Surface Chemistry: Chemical Processes at the Particle-Water Interface*. John Wiley and Sons, New York. 1987.p 255-292, 18 fig, 1 tab, 43 ref.

- Burbank, M., Kavazanjian, E., Weaver, T., Montoya, B. M., Hamdan, N., Bang, S. S., et al. (2013). Biogeochemical processes and geotechnical applications: progress, opportunities and challenges. *Géotechnique*, *63*(4), 287–301. <https://doi.org/10.1680/geotSIP13.P.017>
- Canny, J. (1986). A computational approach to edge detection. *IEEE Transactions on Pattern Analysis and Machine Intelligence*, *6*, 679–698.
- Charlton, S. R., & Parkhurst, D. L. (2011). Modules based on the geochemical model PHREEQC for use in scripting and programming languages. *Computers & Geosciences*, *37*(10), 1653–1663.
- Cunningham, A. B., Class, H., Ebigo, A., Gerlach, R., Phillips, A. J., & Hommel, J. (2019). Field-scale modeling of microbially induced calcite precipitation. *Computational Geosciences*, *23*(2), 399–414.
- Connolly, J., Kaufman, M., Rothman, A., Gupta, R., Redden, G., Schuster, M., et al. (2013). Construction of two ureolytic model organisms for the study of microbially induced calcium carbonate precipitation. *Journal of Microbiological Methods*, *94*(3), 290–299. <https://doi.org/10.1016/j.mimet.2013.06.028>
- Cunningham, A. B., Gerlach, R., Spangler, L., & Mitchell, A. C. (2009). Microbially enhanced geologic containment of sequestered supercritical CO₂. *Energy Procedia*, *1*(1), 3245–3252.
- Cunningham, A. B., Gerlach, R., Spangler, L. M., Mitchell, A. C., Parks, S., & Phillips, A. J. (2011). Reducing the risk of well bore leakage using engineered biomineralization barriers. *Energy Procedia*, *4*, 5178–5185.
- Cuthbert, M. O., Riley, M. S., Handley-Sidhu, S., Renshaw, J. C., Tobler, D. J., Phoenix, V. R., & Mackay, R. (2013). Controls on the rate of ureolysis and the morphology of carbonate precipitated by *S. Pasteurii* biofilms and limits due to bacterial encapsulation. *Ecological Engineering*, *41*, 32–40.
- Dalás, E., Kallitsis, J., & Koutsoukos, P. G. (1988). The crystallization of calcium carbonate on polymeric substrates. *Journal of Crystal Growth*, *89*(2–3), 287–294.
- Davies, C. W., & Jones, A. L. (1955). The precipitation of silver chloride from aqueous solutions. Part 2.—Kinetics of growth of seed crystals. *Transactions of the Faraday Society*, *51*, 812–817.
- Dawe, R. A., & Zhang, Y. (1997). Kinetics of calcium carbonate scaling using observations from glass micromodels. *Journal of Petroleum Science and Engineering*, *18*(3–4), 179–187.
- DeJong, J. T., Mortensen, B. M., Martinez, B. C., & Nelson, D. C. (2010). Bio-mediated soil improvement. *Ecological Engineering*, *36*(2), 197–210.
- Ebigo, A., Phillips, A., Gerlach, R., Helmig, R., Cunningham, A. B., Class, H., & Spangler, L. H. (2012). Darcy-scale modeling of microbially induced carbonate mineral precipitation in sand columns. *Water Resources Research*, *48*, W07519. <https://doi.org/10.1029/2011WR011714>
- Ferris, F. G., Phoenix, V., Fujita, Y., & Smith, R. W. (2004). Kinetics of calcite precipitation induced by ureolytic bacteria at 10 to 20 °C in artificial groundwater. *Geochimica et Cosmochimica Acta*, *68*(8), 1701–1710.
- Fidaleo, M., & Lavecchia, R. (2003). Kinetic study of enzymatic urea hydrolysis in the pH range 4–9. *Chemical and Biochemical Engineering Quarterly*, *17*(4), 311–318.
- Fujita, Y., Redden, G. D., Ingram, J. C., Cortez, M. M., Ferris, F. G., & Smith, R. W. (2004). Strontium incorporation into calcite generated by bacterial ureolysis. *Geochimica et Cosmochimica Acta*, *68*(15), 3261–3270.
- Gal, J.-Y., Bollinger, J.-C., Tolosa, H., & Gache, N. (1996). Calcium carbonate solubility: A reappraisal of scale formation and inhibition. *Talanta*, *43*(9), 1497–1509.
- Ganor, J., & Lasaga, A. C. (1998). Simple mechanistic models for inhibition of a dissolution reaction. *Geochimica et cosmochimica acta*, *62*(8), 1295–1306.
- Graf, D. L. (1961). Crystallographic tables for the rhombohedral carbonates. *American Mineralogist: Journal of Earth and Planetary Materials*, *46*(11–12), 1283–1316.
- Hamdan, N., & Kavazanjian, E. (2016). Enzyme-induced carbonate mineral precipitation for fugitive dust control. *Géotechnique*, *66*(7), 546–555.
- Hammes, F., Boon, N., de Villiers, J., Verstraete, W., & Siciliano, S. D. (2003). Strain-specific ureolytic microbial calcium carbonate precipitation. *Applied and Environmental Microbiology*, *69*(8), 4901–4909.
- Hammes, F., & Verstraete, W. (2002). Key roles of pH and calcium metabolism in microbial carbonate precipitation. *Reviews in Environmental Science and Biotechnology*, *1*(1), 3–7.
- Hill, C. A., Forti, P., & Shaw, T. R. (1997). *Cave minerals of the world*, (Vol. 238). Huntsville: National Speleological Society.
- Hommel, J., Ebigo, A., Gerlach, R., Cunningham, A. B., Helmig, R., & Class, H. (2016). Finding a balance between accuracy and effort for modeling biomineralization. *Energy Procedia*, *97*, 379–386.
- Hommel, J., Lauchnor, E., Phillips, A., Gerlach, R., Cunningham, A. B., Helmig, R., et al. (2015). A revised model for microbially induced calcite precipitation: Improvements and new insights based on recent experiments. *Water Resources Research*, *51*, 3695–3715. <https://doi.org/10.1002/2014WR016503>
- House, W. A. (1981). Kinetics of crystallisation of calcite from calcium bicarbonate solutions. *Journal of the Chemical Society, Faraday Transactions 1: Physical Chemistry in Condensed Phases*, *77*(2), 341–359.
- Kazmierczak, T. F., Tomson, M. B., & Nancollas, G. H. (1982). Crystal growth of calcium carbonate. A controlled composition kinetic study. *The Journal of Physical Chemistry*, *86*(1), 103–107.
- Kim, D., Mahabadi, N., Hall, C., Jang, J., & van Paassen, L. A. (2017). Characterization of calcite mineral precipitation process by EICP in porous media. In AGU Fall Meeting Abstracts.
- Kralj, D., Brečević, L., & Kontrec, J. (1997). Vaterite growth and dissolution in aqueous solution III. Kinetics of transformation. *Journal of Crystal Growth*, *177*(3–4), 248–257.
- Lasaga, A. C. (1981). Rate laws of chemical reactions. *Rev. Mineral; (United States)*, *8*.
- Lauchnor, E. G., Topp, D. M., Parker, A. E., & Gerlach, R. (2015). Whole cell kinetics of ureolysis by *Sporosarcina pasteurii*. *Journal of Applied Microbiology*, *118*(6), 1321–1332. <https://doi.org/10.1111/jam.12804>
- Lebron, L., & Suarez, D. L. (1996). Calcite nucleation and precipitation kinetics as affected by dissolved organic matter at 25 C and pH > 7.5. *Geochimica et Cosmochimica Acta*, *60*(15), 2765–2776.
- Lin, Y. P., Singer, P. C., & Aiken, G. R. (2005). Inhibition of calcite precipitation by natural organic material: kinetics, mechanism, and thermodynamics. *Environmental Science & Technology*, *39*(17), 6420–6428. <https://doi.org/10.1021/es050470z>
- Lioliou, M. G., Paraskeva, C. A., Koutsoukos, P. G., & Payatakes, A. C. (2007). Heterogeneous nucleation and growth of calcium carbonate on calcite and quartz. *Journal of Colloid and Interface Science*, *308*(2), 421–428.
- Mahabadi, N., Zheng, X., & Jang, J. (2016). The effect of hydrate saturation on water retention curves in hydrate-bearing sediments. *Geophysical Research Letters*, *43*, 4279–4287. <https://doi.org/10.1002/2016GL068656>

- Mahabadi, N., Kim, D., Hall, C., Jang, J. & van Paassen, L. A. (2017) Effect of Carbonate Precipitation on the Hydrodynamics of Porous Media: Numerical Simulation, AGU Fall Meeting Abstracts, H13E-1426.
- Martinez, B. C., Barkouki, T. H., DeJong, J. D., & Ginn, T. R. (2011). Upscaling microbial induced calcite precipitation in 0.5 m columns: experimental and modeling results. *Geo-Frontiers 2011: Advances in Geotechnical Engineering* (pp. 4049–4059). Dallas, TX: American Society of Civil Engineers.
- Matty, J. M., & Tomson, M. B. (1988). Effect of multiple precipitation inhibitors on calcium carbonate nucleation. *Applied Geochemistry*, 3(5), 549–556.
- Minto, J. M., Lunn, R. J., & El Mountassir, G. (2019). Development of a reactive transport model for field-scale simulation of microbially induced carbonate precipitation. *Water Resources Research*, 55, 7229–7245. <https://doi.org/10.1029/2019WR025153>
- Mitchell, A. C., & Ferris, F. G. (2006). The influence of *Bacillus pasteurii* on the nucleation and growth of calcium carbonate. *Geomicrobiology Journal*, 23(3–4), 213–226.
- Morse, J. W. (1983). The kinetics of calcium carbonate dissolution and precipitation. *Carbonates: Mineralogy and Chemistry, Reviews in Mineralogy*, 11, 227–264.
- Mortensen, B. M., Haber, M. J., DeJong, J. T., Caslake, L. F., & Nelson, D. C. (2011). Effects of environmental factors on microbial induced calcium carbonate precipitation. *Journal of Applied Microbiology*, 111(2), 338–349. <https://doi.org/10.1111/j.1365-2672.2011.05065.x>
- Mullin, J. W. (2001). *Crystallization* (4th Ed.). Oxford, UK: Butterworth-Heinemann
- Nancollas, G. H., & Reddy, M. M. (1971). The crystallization of calcium carbonate. II. Calcite growth mechanism. *Journal of Colloid and Interface Science*, 37(4), 824–830.
- Nassar, M. K., Gurung, D., Bastani, M., Ginn, T. R., Shafei, B., Gomez, M. G., et al. (2018). Large-scale experiments in microbially induced calcite precipitation (MICP): Reactive transport model development and prediction. *Water Resources Research*, 54, 480–500. <https://doi.org/10.1002/2017WR021488>
- Nemati, M., & Voordouw, G. (2003). Modification of porous media permeability, using calcium carbonate produced enzymatically in situ. *Enzyme and Microbial Technology*, 33(5), 635–642.
- Nielsen, A. E. (1984). Electrolyte crystal growth mechanisms. *Journal of Crystal Growth*, 67(2), 289–310.
- Nielsen, A. E. (1964). *Kinetics of precipitation. International Series of Monographs in Analytical Chemistry* (Vol. 18). Oxford, NY: Pergamon Press.
- Noiriel, C., Steefel, C. I., Yang, L., & Ajo-Franklin, J. (2012). Upscaling calcium carbonate precipitation rates from pore to continuum scale. *Chemical Geology*, 318, 60–74.
- Otsu, N. (1979). A threshold selection method from gray-level histograms. *IEEE Transactions on Systems, Man, and Cybernetics*, 9(1), 62–66.
- Parkhurst, D. L., & Appelo, C. A. J. (2013). Description of input and examples for PHREEQC version 3: A computer program for speciation, batch-reaction, one-dimensional transport, and inverse geochemical calculations. US Geological Survey.
- Perdikouri, C., Piazzolo, S., Kasiopas, A., Schmidt, B. C., & Putnis, A. (2013). Hydrothermal replacement of aragonite by calcite: Interplay between replacement, fracturing and growth. *European Journal of Mineralogy*, 25(2), 123–136.
- Pham, V. P., Nakano, A., Van Der Star, W. R., Heimovaara, T. J., & van Paassen, L. A. (2016). Applying MICP by denitrification in soils: A process analysis. *Environmental Geotechnics*, 5(2), 79–93.
- Phillips, A. J., Gerlach, R., Lauchnor, E., Mitchell, A. C., Cunningham, A. B., & Spangler, L. (2013). Engineered applications of ureolytic biomineralization: A review. *Biofouling*, 29(6), 715–733. <https://doi.org/10.1080/08927014.2013.796550>
- Plummer, L. N., & Busenberg, E. (1982). The solubilities of calcite, aragonite and vaterite in CO₂-H₂O solutions between 0 and 90 °C, and an evaluation of the aqueous model for the system CaCO₃-CO₂-H₂O. *Geochimica et Cosmochimica Acta*, 46(6), 1011–1040.
- Pokrovsky, O. S., Golubev, S. V., & Schott, J. (2005). Dissolution kinetics of calcite, dolomite and magnesite at 25 C and 0 to 50 atm pCO₂. *Chemical geology*, 217(3–4), 239–255.
- Qin, C., Hassanzadeh, S. M., & Ebigbo, A. (2016). Pore-scale network modeling of microbially induced calcium carbonate precipitation: Insight into scale dependence of biogeochemical reaction rates. *Water Resources Research*, 52, 8794–8810. <https://doi.org/10.1002/2016WR019128>
- Reddy, M. M., & Nancollas, G. H. (1973). Calcite crystal growth inhibition by phosphonates. *Desalination*, 12(1), 61–73.
- Roberts, L. (1965). Optical and electro-optical information processing. Cambridge, United States MIT Press.
- Salek, S. S., Bozkurt, O. D., van Turnhout, A. G., Kleerebezem, R., & van Loosdrecht, M. C. M. (2016). Kinetics of CaCO₃ precipitation in an anaerobic digestion process integrated with silicate minerals. *Ecological Engineering*, 86, 105–112.
- Sass, E., Morse, J. W., & Millero, F. J. (1983). Dependence of the values of calcite and aragonite thermodynamic solubility products on ionic models. *American Journal of Science*, 283(3), 218–229.
- Shiraki, R., & Brantley, S. L. (1995). Kinetics of near-equilibrium calcite precipitation at 100 C: An evaluation of elementary reaction-based and affinity-based rate laws. *Geochimica et Cosmochimica Acta*, 59(8), 1457–1471.
- Söhnel, O., & Mullin, J. W. (1982). Precipitation of calcium carbonate. *Journal of Crystal Growth*, 60(2), 239–250.
- Söhnel, O., & Garside, J. (1992). *Precipitation: Basic principles and industrial applications*. Oxford, United Kingdom: Butterworth-Heinemann.
- Stocks-Fischer, S., Galinat, J. K., & Bang, S. S. (1999). Microbiological precipitation of CaCO₃. *Soil Biology and Biochemistry*, 31(11), 1563–1571.
- Tai, C. Y., & Chen, P. (1995). Nucleation, agglomeration and crystal morphology of calcium carbonate. *AIChE Journal*, 41(1), 68–77.
- Terzis, D., & Laloui, L. (2018). 3-D micro-architecture and mechanical response of soil cemented via microbial-induced calcite precipitation. *Scientific Reports*, 8(1), 1416. <https://doi.org/10.1038/s41598-018-19895-w>
- Ubbink, B. J. (2013). Controlled precipitation of calcium carbonate in spatial dimension with multiple calcium chloride and sodium carbonate pulses, Delft University of Technology, Delft, Netherlands.
- Van Paassen, L. A. (2009). Biogrout: Ground improvement by microbially induced carbonate precipitation. *Delft University of Technology*, 64(1), 46–51. <https://doi.org/10.1111/ijj.12061>
- Van Wijngaarden, W. K., Van Paassen, L. A., Vermolen, F. J., Van Meurs, G. A. M., & Vuijk, C. (2016). Simulation of front instabilities in density-driven flow, using a reactive transport model for Biogrout combined with a randomly distributed permeability field. *Transport in Porous Media*, 112(2), 333–359.
- van Paassen, L. A., Ghose, R., van der Linden, T. J. M., van der Star, W. R. L., & van Loosdrecht, M. C. M. (2010). Quantifying biomediated ground improvement by ureolysis: Large-scale biogrout experiment. *Journal of Geotechnical and Geoenvironmental Engineering*, 136(12), 1721–1728.
- van Wijngaarden, W. K., van Paassen, L. A., Vermolen, F. J., van Meurs, G. A. M., & Vuijk, C. (2016). A reactive transport model for biogrout compared to experimental data. *Transport in Porous Media*, 111(3), 627–648.

- van Wijngaarden, W. K., Vermolen, F. J., van Meurs, G. A. M., & Vuijk, C. (2011). Modelling biogrout: A new ground improvement method based on microbial-induced carbonate precipitation. *Transport in Porous Media*, *87*(2), 397–420.
- van Wijngaarden, W. K., Vermolen, F. J., van Meurs, G. A. M., & Vuijk, C. (2012). A mathematical model and analytical solution for the fixation of bacteria in biogrout. *Transport in Porous Media*, *92*(3), 847–866.
- van Wijngaarden, W. K., Vermolen, F. J., van Meurs, G. A. M., & Vuijk, C. (2013). A mathematical model for Biogrout. *Computational Geosciences*, *17*(3), 463–478.
- Wang, Y., Soga, K., Dejong, J. T., & Kabla, A. J. (2019). A microfluidic chip and its use in characterising the particle-scale behaviour of microbial-induced calcium carbonate precipitation (MICP). *Géotechnique*, 1-9.
- Whiffin, V. S. (2004). *Microbial CaCO₃ precipitation for the production of biocement*. Perth, AU: Murdoch University.
- Whiffin, V. S., van Paassen, L. A., & Harkes, M. P. (2007). Microbial carbonate precipitation as a soil improvement technique. *Geomicrobiology Journal*, *24*(5), 417–423.
- Yasuhara, H., Neupane, D., Hayashi, K., & Okamura, M. (2012). Experiments and predictions of physical properties of sand cemented by enzymatically-induced carbonate precipitation. *Soils and Foundations*, *52*(3), 539–549.
- Yoon, H., & McKenna, S. A. (2012). Highly parameterized inverse estimation of hydraulic conductivity and porosity in a three-dimensional, heterogeneous transport experiment. *Water Resources Research*, *48*, W10536. <https://doi.org/10.1029/2012WR012149>
- Zhang, C., Dehoff, K., Hess, N., Ostrom, M., Wietsma, T. W., Valocchi, A. J., et al. (2010). Pore-scale study of transverse mixing induced CaCO₃ precipitation and permeability reduction in a model subsurface sedimentary system. *Environmental Science & Technology*, *44*(20), 7833–7838. <https://doi.org/10.1021/es1019788>
- Zhao, Q., Li, L., Li, C., Li, M., Amini, F., & Zhang, H. (2014). Factors affecting improvement of engineering properties of MICP-treated soil catalyzed by bacteria and urease. *Journal of Materials in Civil Engineering*, *26*(12).
- Zheng, X., Mahabadi, N., Yun, T. S., & Jang, J. (2017). Effect of capillary and viscous force on CO₂ saturation and invasion pattern in the microfluidic chip. *Journal of Geophysical Research: Solid Earth*, *122*, 1634–1647. <https://doi.org/10.1002/2016JB013908>